Lawrence Berkeley National Laboratory

Title

Pore-scale supercritical CO2 dissolution and mass transfer under imbibition conditions

Permalink

https://escholarship.org/uc/item/8r05f868

Authors

Chang, Chun
Zhou, Quanlin
Kneafsey, Timothy J
et al.

Publication Date

2016-06-01

DOI

10.1016/j.advwatres.2016.03.015

Peer reviewed

Pore-scale supercritical CO_2 dissolution and mass transfer under drainage conditions

Author links open overlay panelChunChang[ab]QuanlinZhou[b]MartOostrom[c]Timothy J.Kneafsey[b]HardeepMehta[d]

Show more

Highlights

- Pore-scale drainage and $scCO_2$ dissolution experiments were conducted in a sandstone- analogue pore network.

- A novel fluorescent dye was used for tracking water pH changes with $scCO_2$ dissolution.

- Mechanisms of $scCO_2$ dissolution and mass transfer with dynamic two-phase configurations were observed and analyzed.

- The ratio of interface area to water body volume dominated $scCO_2$ dissolution and mass transfer.

Abstract

Recently, both core- and pore-scale imbibition experiments have shown non-equilibrium dissolution of supercritical CO_2 ($scCO_2$) and a prolonged depletion of residual $scCO_2$. In this study, pore-scale $scCO_2$ dissolution and mass transfer under drainage conditions were investigated using a two-dimensional heterogeneous micromodel and a novel fluorescent water dye with a sensitive pH range between 3.7 and 6.5. Drainage experiments were conducted at 9 MPa and 40 °C by injecting $scCO_2$ into the sandstone-analogue pore network initially saturated by water without dissolved CO_2 ($dsCO_2$). During the experiments, time-lapse images of dye intensity, reflecting water pH, were obtained. These images show non-uniform pH in individual pores and pore clusters, with average pH levels gradually decreasing with time. Further analysis on selected pores and pore clusters shows that (1) rate-limited mass transfer prevails with slowly decreasing pH over time when the $scCO_2$-water interface area is low with respect to the volume of water-filled pores and pore clusters, (2) fast $scCO_2$ dissolution and phase equilibrium occurs when $scCO_2$ bubbles invade into water-filled pores, significantly

enhancing the area-to-volume ratio, and (3) a transition from rate-limited to diffusion-limited mass transfer occurs in a single pore when a medium area-to-volume ratio is prevalent. The analysis also shows that two fundamental processes – $scCO_2$ dissolution at phase interfaces and diffusion of $dsCO_2$ at the pore scale (10–100 μm) observed after $scCO_2$ bubble invasion into water-filled pores without pore throat constraints – are relatively fast. The overall slow dissolution of $scCO_2$ in the millimeter-scale micromodel can be attributed to the small area-to-volume ratios that represent pore-throat configurations and characteristics of phase interfaces. This finding is applicable for the behavior of dissolution at pore, core, and field scales when water-filled pores and pore clusters of varying size are surrounded by $scCO_2$ at narrow pore throats.

Keywords

Geological carbon sequestration
Micromodel
Drainage
Dissolution
Mass transfer

1. Introduction

Dissolution trapping, along with structural and stratigraphic trapping, residual trapping, and mineral trapping, is critical to the permanent containment of injected supercritical CO_2 ($scCO_2$) in saline aquifers (IPCC, 2005). The dissolution of injected $scCO_2$ occurs within $scCO_2$ plumes under drainage conditions by local phase partitioning, beneath $scCO_2$ plumes by convection induced by the density difference between resident brine without and with dissolved CO_2 ($dsCO_2$), and along immobile, tailing edges of $scCO_2$ plumes under imbibition conditions by the influence of ambient groundwater flow (Chang et al., 2014). Here, dissolution is referred to as the change of $scCO_2$ to $dsCO_2$ at $scCO_2$-water phase interfaces, with the solubility determined by given pressure, temperature and salinity, and is generally assumed to be instantaneous; mass transfer is referred to as the transport of $dsCO_2$ away from these interfaces to water-filled pores and pore clusters, including advection, dispersion, and diffusion, taking their geometry into consideration.

Recently, local dissolution of $scCO_2$ and mass transfer of $dsCO_2$ under imbibition conditions have been investigated by injecting $dsCO_2$-undersaturated water into post-drainage core samples (Akbarabadi and Piri, 2013, Berg et al., 2013, Chang et al., 2013, Chang et al., 2014) and into a sandstone-analogue, heterogeneous micromodel

(Chang et al., 2016). Common to all these experiments is the prolonged depletion of residual scCO$_2$, contrary to rapid depletion expected when a local, instantaneous phase equilibrium is assumed (e.g., Spycher and Pruess, 2005, Pruess and Spycher, 2007, Zhou et al., 2008, Zhou et al., 2010). The observed non-equilibrium dissolution can be attributed to the limited interactions between mobile water and immobile scCO$_2$ at the scale of individual pores, pore clusters, and pore networks (Chang et al., 2016) and at the scale of core samples (Akbarabadi and Piri, 2013). For example, a limited number of water flow paths were imaged over the entire pore network under various experimental conditions, slowing down the dissolution of by-passed clusters of residual scCO$_2$ bubbles (Chang et al., 2016). Therefore, it is important to understand the dynamic configurations between mobile water and immobile scCO$_2$ at multiple scales. The non-equilibrium scCO$_2$ dissolution is more important under drainage conditions than imbibition conditions. It may affect scCO$_2$ migration and dsCO$_2$trapping in a plume over hundreds of km^2 for an industrial-scale storage project (Zhou et al., 2010, Birkholzer et al., 2015). To the best of our knowledge, there has been only one laboratory experiment of scCO$_2$ dissolution conducted under drainage conditions (Berg et al., 2013). They found a significant difference in time-dependent scCO$_2$ saturation distribution when injecting scCO$_2$ into a relatively homogeneous core initially saturated by dsCO$_2$-saturated and dsCO$_2$-free water. However, they arbitrarily attributed the small difference in core-scale average saturation between the two scenarios to scCO$_2$ dissolution at equilibrium. Local scCO$_2$ dissolution may also affect enhanced dissolution by convection. So far, all studies of convection-enhanced dissolution have assumed the presence of a boundary layer of dsCO$_2$ at solubility at the top of study domain in numerical simulations (e.g., Ennis-King and Paterson, 2005, Riaz et al., 2006, Pau et al., 2010) or have introduced gaseous CO$_2$ or an analogue fluid into an aperture in 2D Hele-Shaw cells or packed sands or glass beads in 1D columns or 2D sand tanks (Kneafsey and Pruess, 2010, Agartan et al., 2015). The non-equilibrium dissolution may result in dsCO$_2$ concentration in the boundary layer that slowly increases with time before reaching solubility, leading to the non-instantaneous dissolution at certain spatial scales. This slow process will affect the development of a stable, diffusion-dominant boundary layer of dsCO$_2$-containing brine, the onset and initialization of unstable fingers of dsCO$_2$ originating from the boundary layer, and the evolution, merging, and decay of these fingers in both homogeneous and heterogeneous porous media (Ennis-King and Paterson, 2003, Kneafsey and Pruess, 2010, Neufeld et al., 2010, Backhaus et al., 2011, Aggelopoulos and Tsakiroglou, 2012, MacMinn et al., 2012, Agartan et al., 2015).

In this study, we focused on the dynamic dissolution of scCO$_2$ in different phase configurations of water-filled pores and pore clusters. We injected scCO$_2$ into an initially water-saturated heterogeneous micromodel (a sandstone-analogue), with the intent to image the pH of residual water. The pore network was initially saturated with dyed dsCO$_2$-free water. Time-lapse images of fluorescent intensity in the water phase (water intensity) were obtained using a pH-sensitive fluorescent water dye and a fluorescence imaging system. The water intensity is related to the number of photon emissions from the fluorescent dye in water phase occurring when the fluorescent molecules relax to their ground state after excitation. For the pH sensitive dye used in this study, lower pH results in higher intensity. Through the relationship between water intensity, water pH value and thus dsCO$_2$ concentration, we directly observed the transient dissolution and mass transfer processes at the pore scale, and over the entire micromodel.

2. Materials and methods

2.1. Micromodel

The micromodel used in our study was similar to that used by Zuo et al. (2013)and Chang et al. (2016). The pore configuration of the two-dimensional (2D) model was converted into a photomask from section micrographs of a Mt. Simon sandstone core extracted from an injection well of the Illinois Basin - Decatur project (Senel et al., 2014). Based on the photomask, a silicon wafer micromodel was fabricated using standard photolithography, coupled plasma-deep reactive ion etching (ICP-DRIE), thermal oxidation, and anodic bonding (Chomsurin and Werth, 2003, Willingham et al., 2008). The porous medium portion consists of nine identical sub-images in a 3 × 3 array, with a total area of 7.1 mm × 5.3 mm and 35 μm in depth. The pore network has a porosity of 0.35 and a pore volume (PV) of 0.461 μL. The absolute permeability of the micromodel is 5.3 × 10^{-13} m^{2}measured at ambient pressure and temperature. Additional details and an image of the micromodel can be found in Chang et al. (2016).

2.2. Experimental procedures

A high-pressure, high-temperature experimental setup was used for the drainage and dissolution experiments. Detailed descriptions and schematics of the system can be found in the supplementary material and in Chang et al., 2016, Wang et al., 2013, and Zhang et al. (2011). The micromodel was emplaced in a high-pressure cell containing glycerol, with a sapphire viewing window. To establish the initial conditions, gaseous CO$_2$ was first injected into the micromodel to displace air from the micromodel

and tubing. De-ionized (DI) water was then injected to dissolve and displace the gaseous CO_2 to achieve a water-saturated system. In the subsequent step, a total of 1.5 mL DI water containing the pH-dependent dye pHrodo Red (pHrodo® Red AM Intracellular pH Indicator, Life Technologies, Carlsbad, CA) was injected to displace the dye-free water. The utility of the pH-dependent dye is explained in more detail in Section 2.3. After these steps were conducted under atmospheric conditions, the system pressure was gradually increased to 9.0 MPa (with a confining pressure of 9.58 MPa) and the temperature was raised to 40 °C. The system was heated to the experimental temperature using a temperature chamber (In Vivo Scientific, St. Louis, Mo) by circulating hot air. The temperature of the pump cylinders and fluid delivery pipelines are controlled by circulating hot water from a water heater (Fisher Scientific). The initial conditions were established after more than 100 PVs of dyed water were injected into the micromodel by keeping phase CO_2 under supercritical conditions. In the system, fluids were injected by using a total of four ISCO syringe pumps (Teledyne ISCO Inc., Lincoln, NE).

A major design criterion for the drainage experiments is the creation of low residual water saturation conditions, allowing dissolution and mass transfer evaluations at individual pores or pore clusters. Preliminary experiments showed that the lowest residual water saturations could be obtained at $scCO_2$ injection rates of 2500 µL/h. The application of higher rates did not reduce the residual saturation levels and injection at lower rates resulted in considerably higher water saturations with relatively large zones of bypassed water. The injection rate of 2500 µL/h was also selected to shorten the duration of the drainage process; this rate is consistent with the rates used by Zhang et al. (2011) and Wang et al. (2013) for similar size micromodels and experimental conditions. High injection rates are also common in core-flooding experiments as a means to demonstrate flow and transport phenomena in a reasonable experimental time (e.g., Shi et al., 2011, Akbarabadi and Piri, 2013, Pini and Benson, 2013a, Pini and Benson, 2013b).

The application of the 2500 µL/h $scCO_2$ injection rate resulted in a good reproducibility in terms of residual water saturations (Fig. 1). For each of the three drainage tests under identical conditions shown in Fig. 1, the pore-network was equally divided into ten vertical slices (0.71 mm × 5.3 mm) perpendicular to the flow direction. After segmentation using a threshold value of 3000, water saturations at the end of the experiment were calculated for each slice. The average residual water saturations of the three experiments were 0.176, 0.182, and 0.205. The figure shows that residual saturations are comparable for the three experiments and that residual saturation

increases with distance from the inlet. The increases in saturation with travel distance are related to the occurrence of capillary end effects in combination with the relatively small size of the micromodel. The capillary end effect results from a discontinuity in capillary pressure at the ends of the media, and tends to make it difficult for the wetting phase to leave the porous media, leading to a higher water saturation in the down gradient region of the system. Similar end effects are common and have been reported for micromodels (Rodriquez de Castro et al., 2015, Rodriguez de Castro et al., 2016, Wang et al., 2013) and column experiments (Krevor et al., 2012, Pini et al., 2012). The drainage and dissolution experiments were conducted for over 4.5 h, resulting in a total injection of almost 8500 PVs. The $scCO_2$ displacement occurred fairly rapidly due to the high injection rate used. The first image taken at 10 min after injection showed the completion of $scCO_2$ displacement, and the residual water saturation remained relatively constant until the end of the experiments (274 min). Because of the similarity in residual water distribution and saturation over the three experiments, the experiment resulting in an average residual water saturation of 0.182 was selected for detailed analysis of $scCO_2$ dissolution and mass transfer into distinct pores and pore clusters.
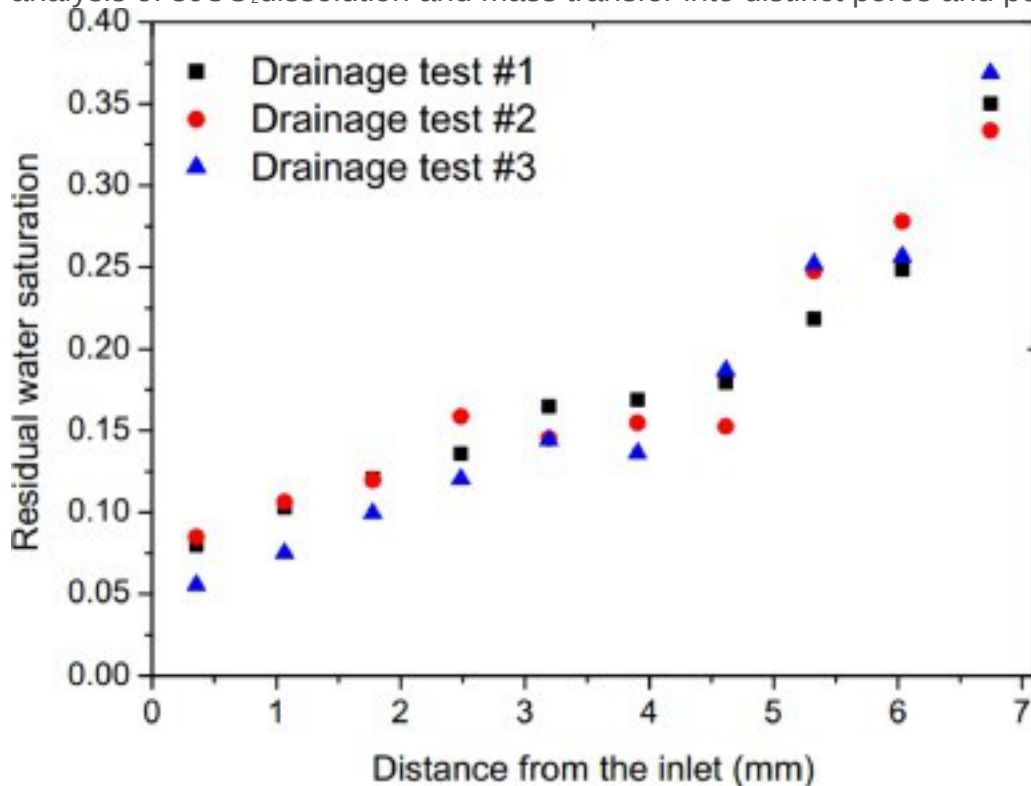

Fig. 1. Average residual water saturation as a function of the distance from the inlet of the micromodel for the three drainage experiments under identical experimental conditions.

2.3. Fluorescence imaging

A fluorescence imaging system was used to [measure water](#) intensity during the drainage and dissolution experiments. A new fluorescent pH indicator, pHrodo Red, was used to observe the water pH during $scCO_2$ dissolution and mass transfer. pHrodo Red is weakly fluorescent at neutral pH but becomes increasingly fluorescent as the pH decreases, with an advertised functional pH range between 4 and 9 ([Life Technologies Website](#)). The imaging system with the pHrodo Red dye was calibrated to establish the relationship between pH and water intensity. For this purpose, six pH solutions between 3.70 and 6.50 were prepared with [hydrochloric acid](#), using a constant dye concentration of 8 µmol/L. This concentration maximized the intensity range of our fluorescence system. For calibration, each pH solution was injected into the micromodel at 9.0 MPa and 40°C. After injection of more than 100 PVs, three scans were taken at 10 min intervals and the average water intensity was calculated. [Fig. 2](#) shows the calibration relationship between water intensity and pH, as well as their (small) standard deviation. The mean water intensity varies from 3700 at a pH of 6.50 to the maximum value of 16,200 at a pH of 3.7. The equation shown in the figure was used to convert intensity to pH values. It should be noted that for our application, the primary interest was in the pH range from neutral to pH = 3.1, indicating solubility at the 9.0 MPa and 40°C experimental conditions ([Spycher et al., 2003](#)). A number of promising dyes were tested but only this particular dye yielded consistent calibration curves. Given that the lowest reliable level for this dye was pH = 3.7, which is 0.6 units larger than the pH at solubility, it is obvious that the application is not perfect. However, to the best of our knowledge, no other pH-dependent dye has been described in the literature for [pore-scale](#) experimental studies involving water and $scCO_2$, justifying presentation of our experimental results.
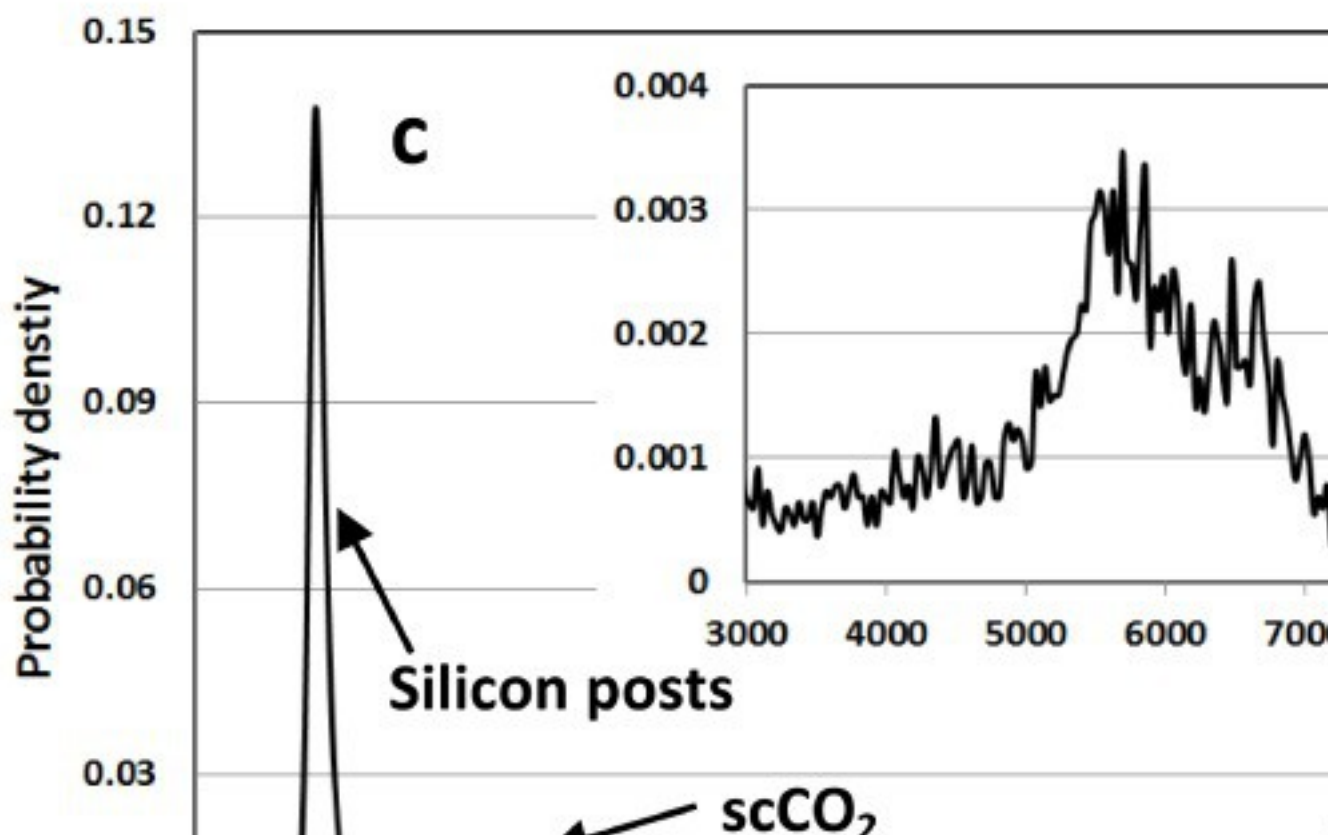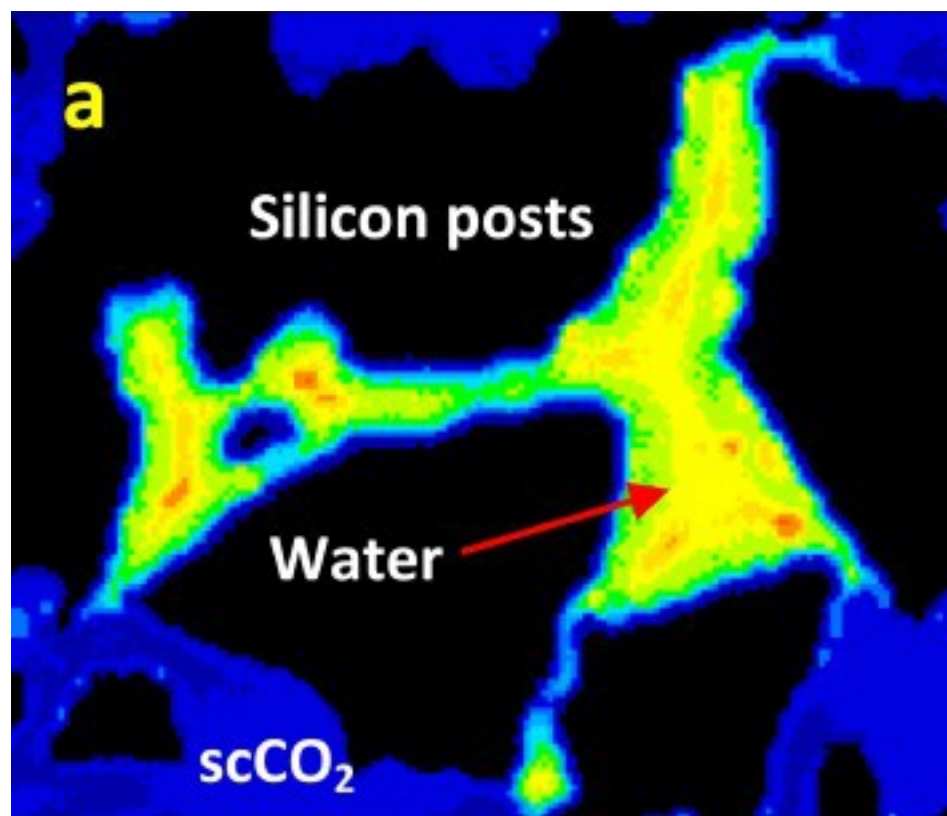
$$y = 6.71 \times \left(1 - \frac{7.26}{118933} x\right)^{\frac{1}{7.26}}$$

$$R^2 = 0.9952$$
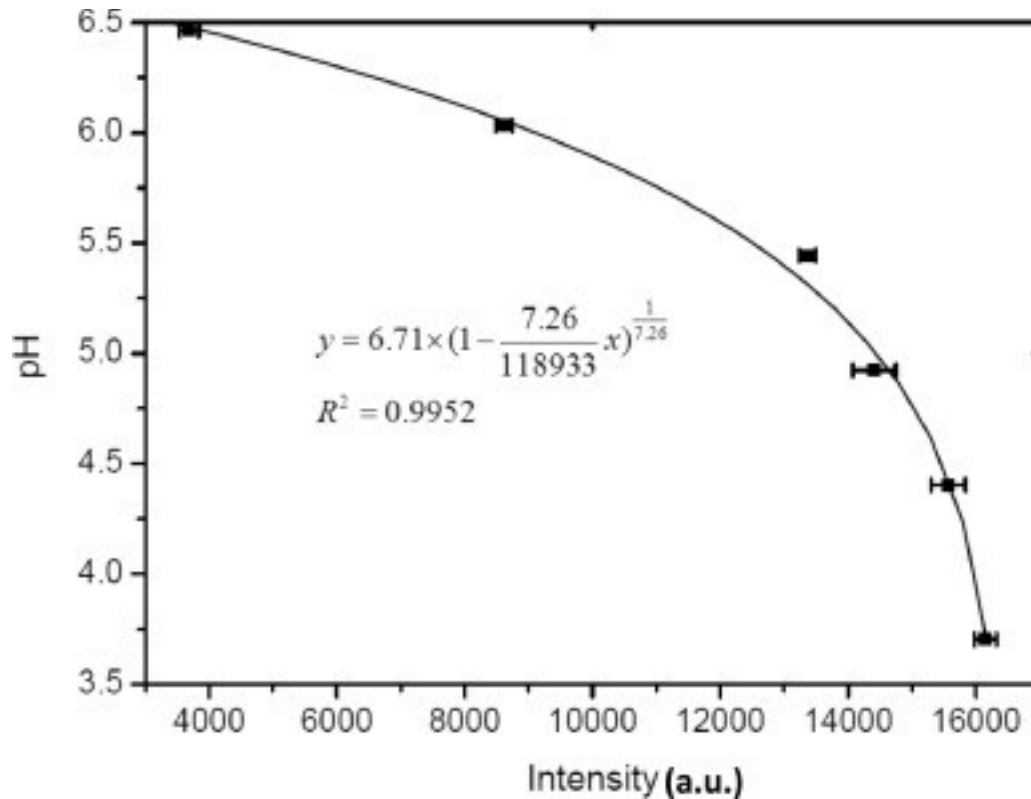
1. Download high-res image (109KB)
2. Download full-size image

Fig. 2. Relationship between pH and dyed-water intensity for the pHrodo Red dye at 8 μmol/L. The equation was used to compute pH values from measured water intensities.

Fluorescent images were acquired using a Nikon Eclipse TE2000-E epifluorescent microscope (Melville, NY) through a 4X inverted objective with a resolution of 1.62 μm/pixel, and the dye intensity was obtained through a Tritc (λ_{ex} = 532–554 nm, λ_{em} = 570–613 nm) filter set. The excitation and emission wavelength of the pH indicator was 550 and 585 nm, respectively. A single image of the pore network is a montage of 15 (5 × 3) separate sub-images acquired using a CoolSnap HQ2 monochrome CCD camera (Photometrics Inc., Tucson, AZ). The camera was controlled by a computer and imaging software (NIS-Elements, Nikon, Melville, NY). During imaging, exposure time of light source affects the intensity signal from the dye in water phase. To keep consistency during system calibration and drainage experiments, the same exposure time was used and eight images with different time intervals were obtained during the scCO$_2$ drainage and dissolution phases.

Segmentation and analysis of the images were conducted using the ImageJ, a public domain JAVA based software (Rasband, 1997–2014). Phase saturations were

computed using intensities of 650–990 (silicon grains), 1500–2300 ($scCO_2$), and >3000 (water), allowing for a precise segmentation of water from $scCO_2$ and grains. The threshold value of 3000 was used for water without $dsCO_2$ and higher values indicate that pore water contains $dsCO_2$. Fig. 3 shows an example of a water-filled pore, surrounded by $scCO_2$ and silicon posts, during a drainage experiment. Fig. 3a illustrates clear differences between the phases, allowing for phase saturation analysis computations using binary images. Fig. 3b shows an example of a binary image illustrating water saturation after segmentation with a threshold value of 3000. For completeness, the associated histogram of probability density vs. intensity in Fig. 3c shows distinct ranges in values for the materials of interest. The lower water intensity along the silicon grain surfaces and in the narrow pore throats (see Fig. 3a) can be attributed to the lateral smoothing caused by the low grain intensity and by the deviation of the true thickness of these fabricated surfaces and pore throats from the typical designed values. These effects were considered when calculating the probability density curve in Fig. 5.

a

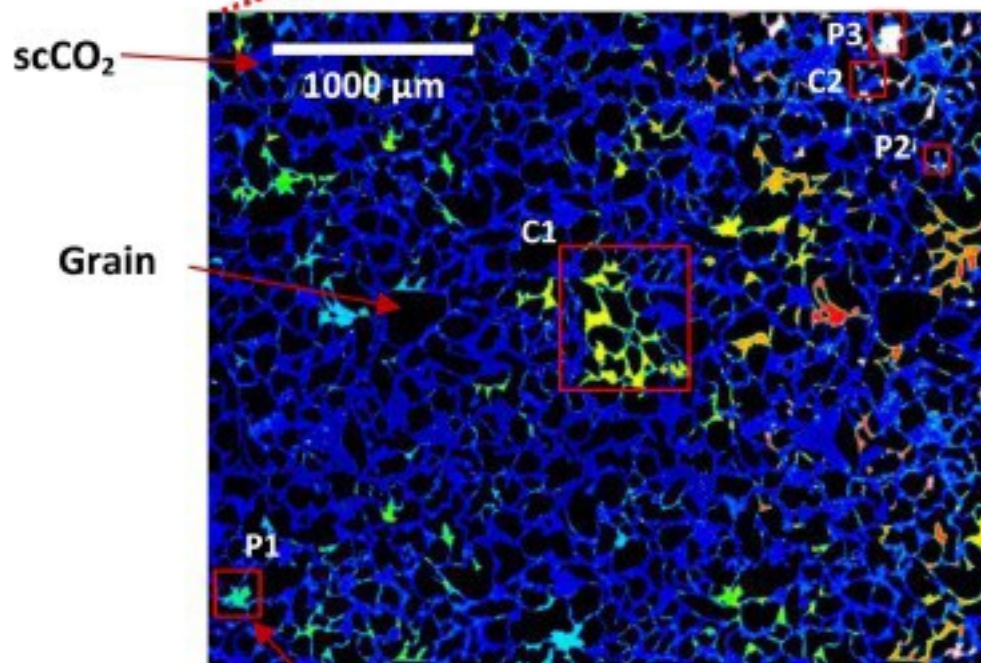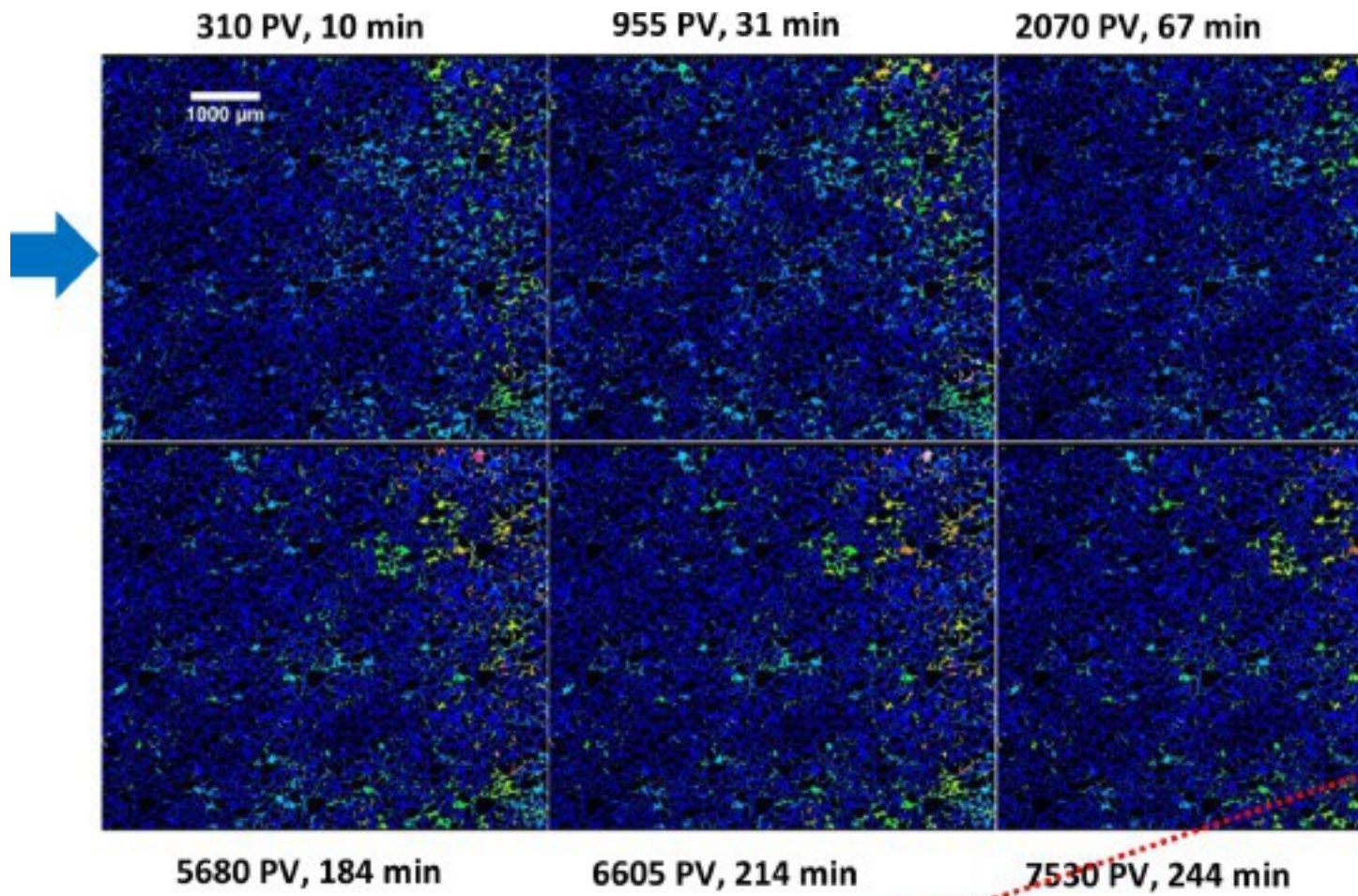Silicon posts

Water

scCO₂

b

c

Probability denstiy

0.15

0.12

0.09

0.06

0.03

Silicon posts

scCO₂

0.004

0.003

0.002

0.001

0

3000   4000   5000   6000   700

Fig. 3. (a) Example image demonstrating the intensity distribution for $scCO_2$ (blue), dyed water (green to red), and silicon posts (black), (b) binary image, after segmentation with a threshold intensity value of 3000 to indicate presence of water, and (c) histogram of probability density vs. intensity showing silicon posts, $scCO_2$ and water. The water intensity with $dsCO_2$ for the example is further identified in the insert. (For interpretation of the references to color in this figure legend, the reader is referred to the web version of this article.)

3. Results and discussion

3.1. Transient intensity and water pH

Fig. 4 shows eight fluorescence images of fluid distribution for different cumulative $scCO_2$ injection volumes and times. These images illustrate the changes in water pH over the whole pore network after the displacement of water by $scCO_2$ was completed (i.e., at residual water saturation). The first image is taken at 10 min (310 PV of injected $scCO_2$) while the final image is obtained at the end of the experiment at 274 min (8455 PV). During drainage, the dyed water in large pores and throats has been displaced by $scCO_2$, resulting in an average water saturation of 0.182 at 10 min. After that, water saturation remains stable with computed changes within the margins of error.

310 PV, 10 min   **955 PV, 31 min**   **2070 PV, 67 min**

5680 PV, 184 min   **6605 PV, 214 min**   **7530 PV, 244 min**

scCO₂

Grain

P3
C2
P2
C1
P1

1000 µm

Fig. 4. Images of water pH interpreted from intensity values (>3000) and $scCO_2$ and grain posts at eight different pore volumes of injected $scCO_2$ and injection times. In the images, $scCO_2$ has an intensity of 1500–2300 (blue) and solid grains have a range from 650–990 (black). The blue arrow indicates the flow direction of injected $scCO_2$. The magnification shows the locations of three selected pores (P1, P2, and P3) and two clusters (C1 and C2) used for interpretation of dissolution and mass transfer mechanisms. Note the increased saturation of water (brighter pores) towards the effluent end of the micromodel. (For interpretation of the references to color in this figure legend, the reader is referred to the web version of this article.)

The distribution of residual water during the drainage process can be clearly observed from the images in Fig. 4, where computed water pH values are shown. For these images and subsequent pore network figures, the black and blue colors are used to indicate the presence of micromodel grains and $scCO_2$, respectively, similar to Fig. 3. Consistent with the quantitative information shown in Fig. 1, the images in Fig. 4 show that the residual water is mainly located in the downstream portion of the micromodel and along 2–3 paths in the upstream portion. At the pore scale, the residual water is present in both individual pores and pore clusters by-passed by injected $scCO_2$, as shown in the magnified image in Fig. 4. These water-filled pores and pore clusters may have relatively large pore sizes, but have small pore throats connecting to the flow paths of injected $scCO_2$. The pH in these pores and pore clusters are non-uniform through the entire micromodel, and values were generally larger in the downstream portion. The pH decreased gradually with time, but at different rates in the various pores and pore clusters. Even at the end of the experiment after 4.5 h, the pH in the majority of the water-filled pores and pore clusters was still higher than the minimum allowable pH value of 3.7 (Fig. 2), indicating that it takes a relatively long time for $scCO_2$dissolution and $dsCO_2$ mass transfer to occur at the pore scale, particularly considering the spatial scale and lack of chemical reactions.

To understand the statistics of the distribution of water pH for each image and the changes in the distribution among different images, we computed the pH probability density function using over 220,000 pixel values at a constant number (64) of intervals. First, the number of pixels for each intensity interval (thus pH value) was counted. Then, the ratio of associated pixel number to the total 220,000 was calculated. Finally, the histogram of pH values and their corresponding pixel ratios, representing the pH probability density function, was plotted. Fig. 5 shows the probability density histogram

for the eight images shown in Fig. 4. For the first image (at 10 min), the histogram shows a single peak at the interval probability of 0.039 and a pH of 6.47, with a range from 6.5 to 3.7. This indicates that almost all water-filled pores are undersaturated with $dsCO_2$ after 10 min (310 PV of injected $scCO_2$). As $scCO_2$ injection continues, the peak probability decreases with a corresponding decrease in pH, suggesting that $scCO_2$ dissolution and $dsCO_2$ mass transfer continues over time. For the 4th image (at 97 min), for example, besides a peak probability of 0.026 for a pH of 6.45, an additional peak with a probability of 0.012 and pH of 6.29 is present. A third peak at a pH of 5.61 appears in the final image at the end of the experiment, indicating that the $dsCO_2$ concentration in some water-filled pores and pore clusters has increased significantly. In addition, there is a remarkable probability, as high as 0.009, at the end of the drainage for pixels having a pH lower than 4.00. Overall, at the end of the experiment after 4.5 h of $scCO_2$ injection, 91% of the water pixels show a pH higher than 5.90 and only less than 1% reached the minimum value of 3.70, as shown by the cumulative probability curves in Fig. 6. The numbers indicate that the process for $dsCO_2$ concentration to reach solubility value at the pore scale is long-term, even in the millimeter-scale micromodel.
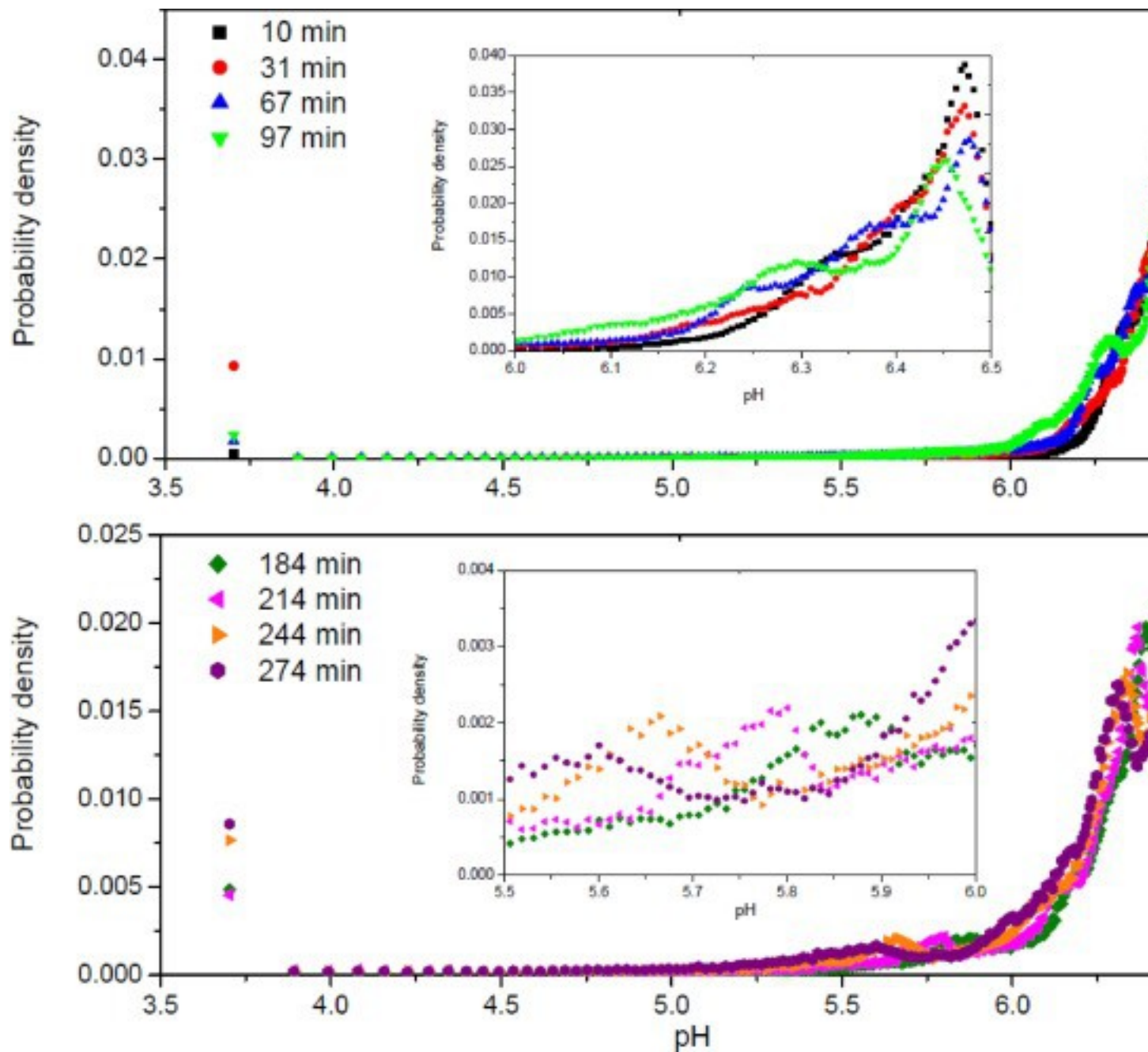
Fig. 5. Histogram of probability density vs. pH for water-filled pores in the entire micromodel for eight imaging times.
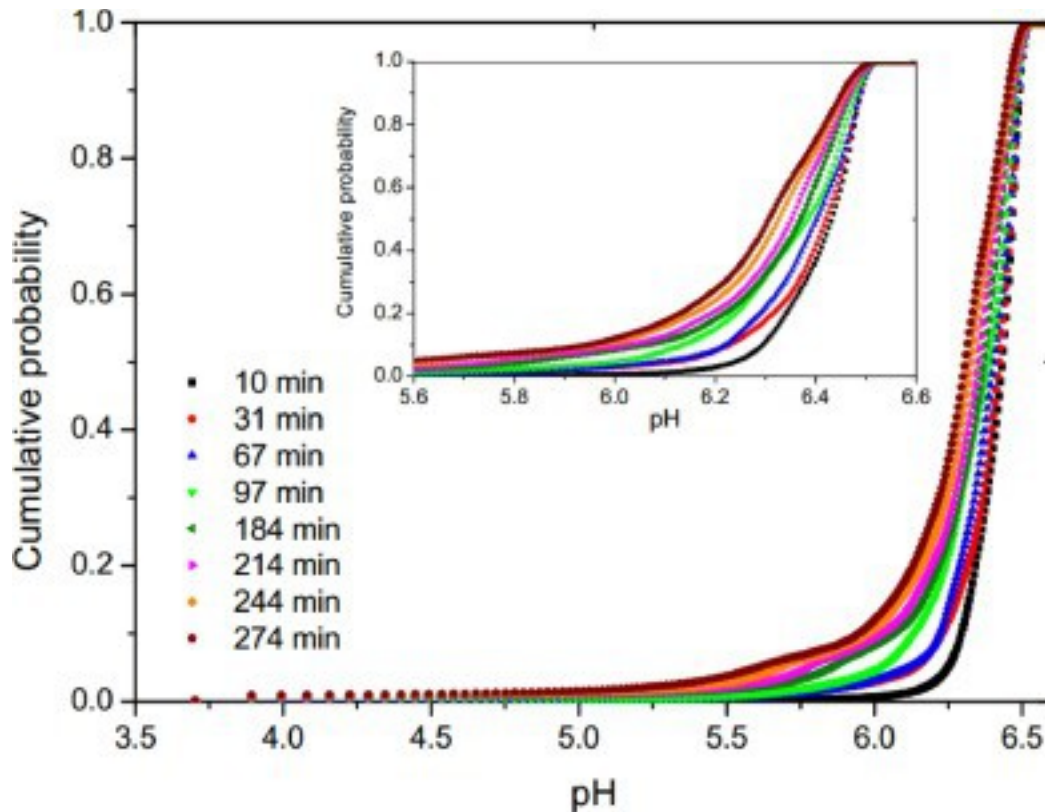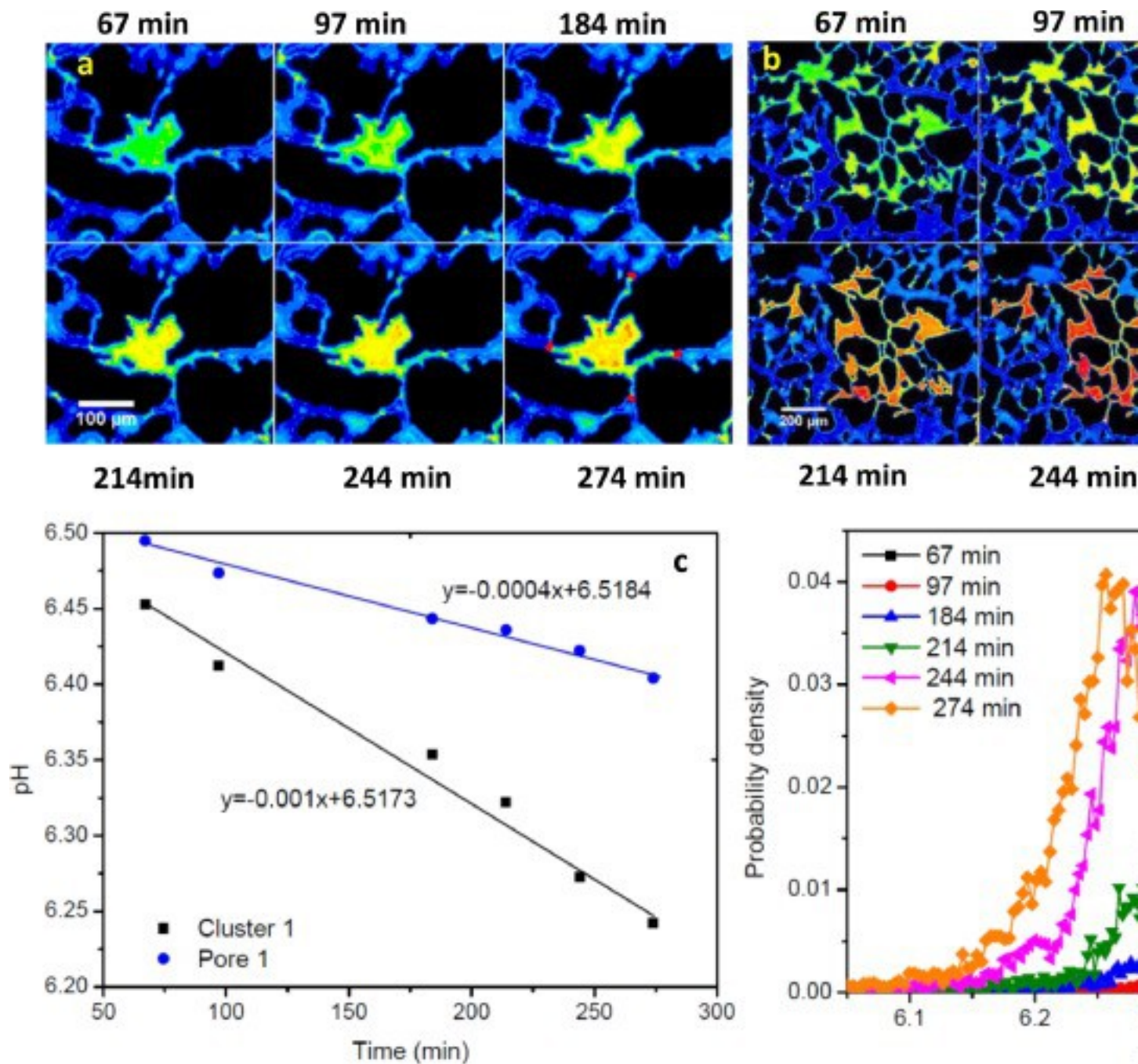
Fig. 6. Histogram of cumulative probability vs. pH for water-filled pores in the entire micromodel for different imaging times.

The observed prolonged process of scCO$_2$ dissolution and dsCO$_2$ mass transfer at the pore scale can be explained by analyzing the transient pH changes at the scale of individual pores and pore clusters filled by dyed water. The detailed analysis was conducted for five selected water-filled pores or pore clusters that are connected by surrounding scCO$_2$-filled pores via pore throats of different configurations (Fig. 4), followed by an analysis for over 100 selected water-filled pores and pore clusters. Through these examples, we will illustrate that the relevant physical processes including scCO$_2$ dissolution at scCO$_2$-water interfaces, mass transfer of dsCO$_2$ from the interfaces along water-filled pore throats to the edges of water-filled pores, and dsCO$_2$ diffusion from these edges to pore centers.

3.2. Rate-limited mass transfer

A single pore (P1 in Fig. 4) and a single cluster of pores (C1 in Fig. 4) filled with dyed-water were selected to demonstrate rate-limited mass transfer of dsCO$_2$ from stable scCO$_2$-water phase interfaces into a water-filled pore or cluster. As shown in Fig. 7a and

c, the pH in the single pore is relatively uniform in each of the six images at different injection times, and the average pH over the entire pore slowly decreases from 6.50 at 67 min to 6.40 at 274 min. For this configuration, the pore throats are also water-filled, and the stable $scCO_2$-water interfaces are located at the connecting $scCO_2$-filled pores, as marked with pink lines in the last image of Fig. 7a. The slow decrease in the average pH with time is attributed to a small $scCO_2$ dissolution rate at the phase interfaces, which are characterized by a small value of the ratio (0.0039/μm) of the phase interfacial areas to the volume of the water-filled pore (a_{it}). Assuming a constant pore-network depth, a_{it} values are computed by dividing the length of $scCO_2$-water interfaces by the water surface areas. Although for the configurations in Fig. 7 dissolution at the $scCO_2$-water interfaces may be a relatively fast process, the integrated total mass flow into the pore is relatively slow due to the small a_{it}.

Fig. 7. Time-lapse images of water pH for (a) a single [pore](#) (Pore 1) and (b) a cluster of pores (Cluster 1) with small a_t values. Also shown are (c) the temporal change in average pH for the entire pore and cluster, and (d) histogram of probability density vs. pixel pH at different times for Cluster 1. The pink lines in (a) indicate scCO$_2$-water interfaces and the white dotted line in (b) shows the boundary of the water-filled cluster.

1. [Download high-res image (1MB)](#)
2. [Download full-size image](#)

Similar behavior of scCO$_2$ dissolution and dsCO$_2$ mass transfer was also observed in Cluster 1, which consists of more than 10 water-filled pores (Fig. 7b). The pH in each of the six images also has a small variability over the entire pore cluster, as shown by the distributions of the probability density of pixel pH (Fig. 7d). The small overall variability is likely caused by different dissolution at the various interfaces, and by the difference between pixel intensity in pores and pore throats within the cluster. The average pH for the entire cluster gradually decreases from 6.45 at 67 min to 6.24 at 274 min, which is slightly faster than that for Pore 1 (Fig. 7c). This higher rate is consistent with a higher a_{it} of 0.0061/μm for Cluster 1, indicating the importance of the total interfacial area on dsCO$_2$ mass transfer from phase interfaces to the pore centers.

For both pore configurations shown in Fig. 7, the pore-scale imaging with the pH dye directly captured the slow processes of scCO$_2$ dissolution and dsCO$_2$ mass transfer in a single pore or pore cluster with small a_{it} values. The slow processes can be attributed to the rate-limited mass transfer of dsCO$_2$ into the single pore and cluster after dissolution of scCO$_2$ at the phase interfaces at pore throats. The direct evidence of the prolonged time scale for dsCO$_2$ at the pore scale to reach equilibrium under drainage conditions is consistent with the indirect evidence shown in previous studies at the core scale under imbibition conditions (Chang et al., 2013, Chang et al., 2014). These previous experiments demonstrated that non-equilibrium dissolution prevails when water free of dsCO$_2$ is injected into cores with residual scCO$_2$ saturation, and that long periods of time are needed to completely deplete the residual scCO$_2$ mass via dissolution and mass transfer.

3.3. Fast scCO$_2$ dissolution and phase equilibrium

In contrast to the above two cases with stable scCO$_2$-water interfaces and small a_{it} values, we selected a single pore (P2 in Fig. 4) and a pore cluster (C2 in Fig. 4) to investigate enhanced dissolution and mass transfer by invasion of a scCO$_2$ bubble into the water-filled pore and cluster. As shown in Fig. 8a and b, the relatively uniform pH in Pore 2 gradually decreased with time during the first 97 min of injection. However, after a scCO$_2$ bubble invaded the water-filled pore, the pH in the segregated water bubbles rapidly decreased to 3.70 in less than 1.5 h, indicating that CO$_2$ dissolution at the scCO$_2$-water interfaces, along with diffusion of dsCO$_2$ to the pore centers, is a much faster process than for Pore 1. The actual pH is likely lower, but 3.70 is the lowest value that could be obtained with the pHrodo Red dye. The change in pH over time (Fig. 8d) is attributed to the change in the a_{it} values caused by the scCO$_2$ bubble invasion. The value increased from 0.0043/μm before the scCO$_2$ bubble invasion to 0.028/μm at 184 min, finally reaching 0.14/μm after segregation of the water bubbles at 274 min.
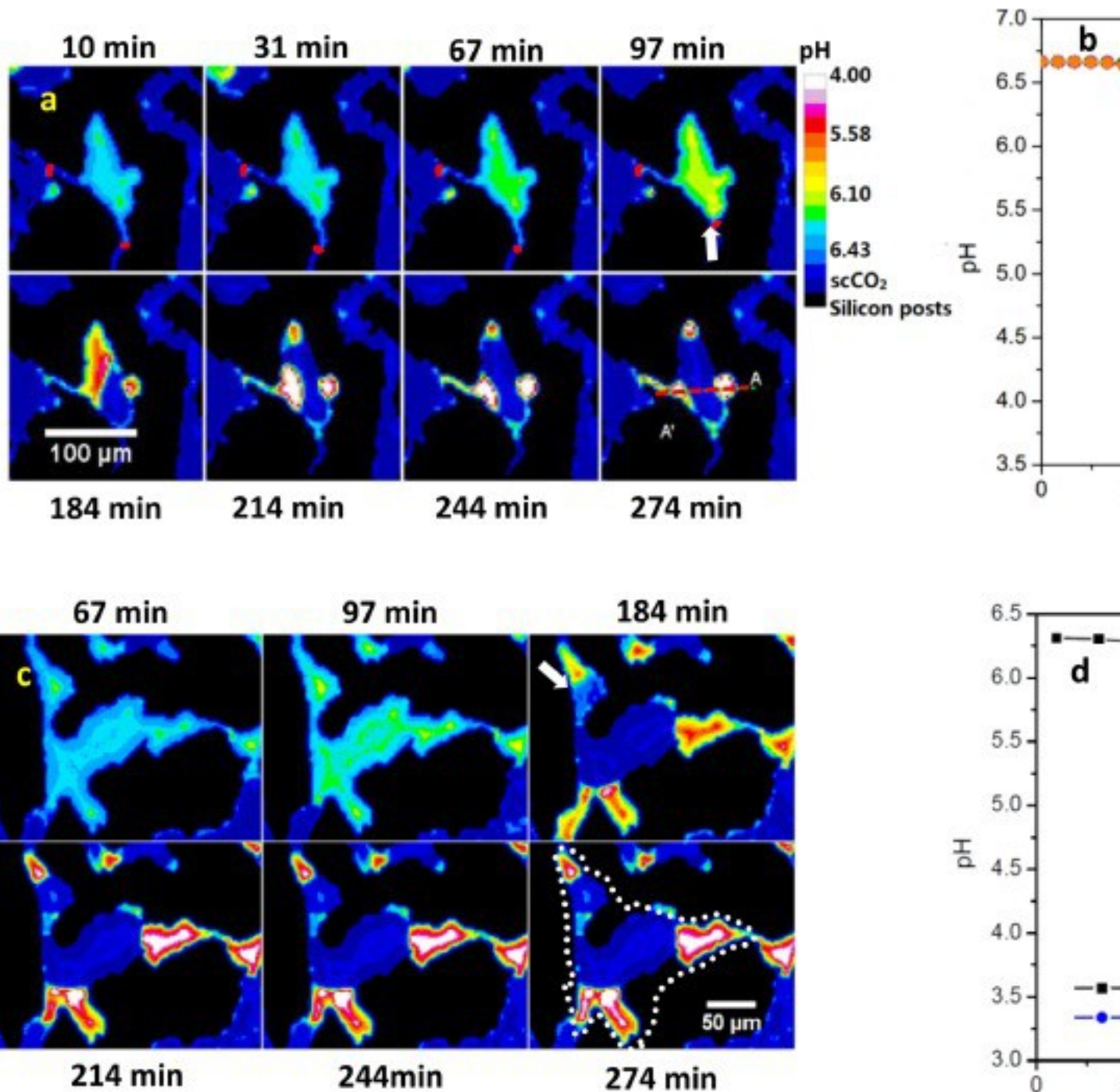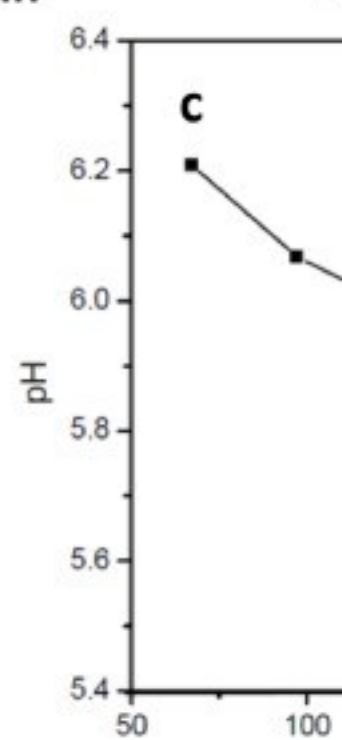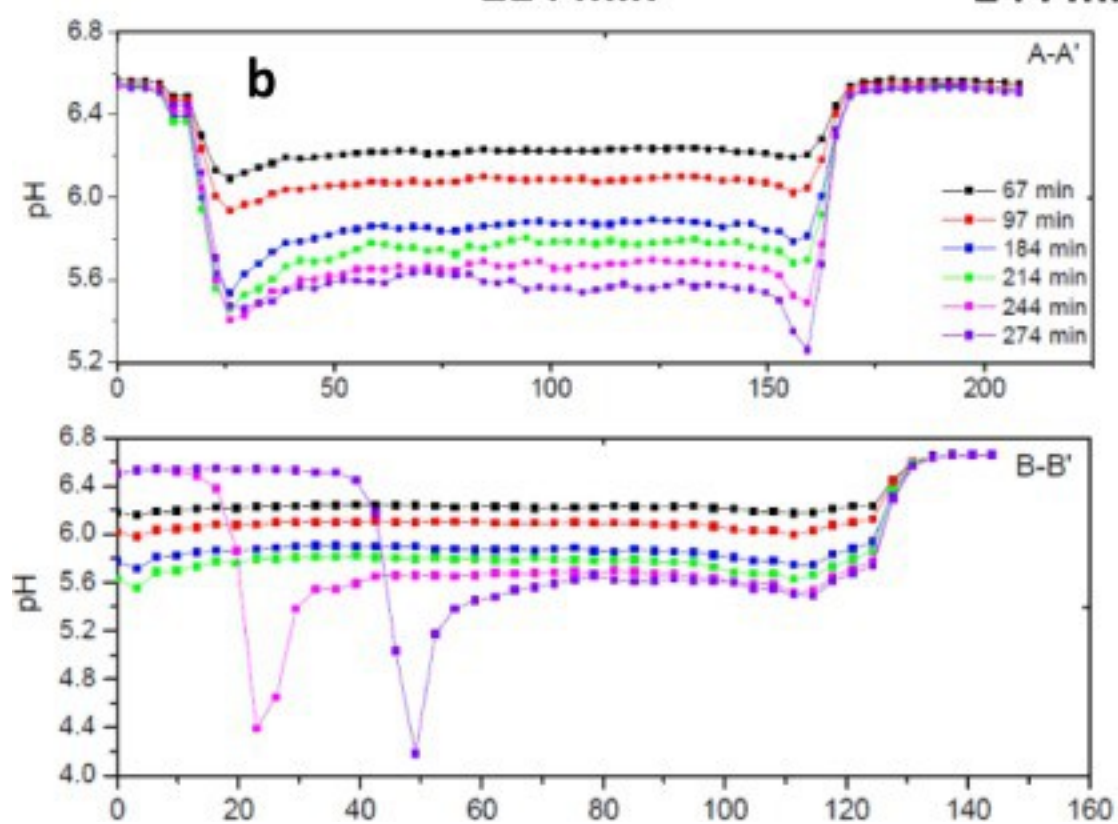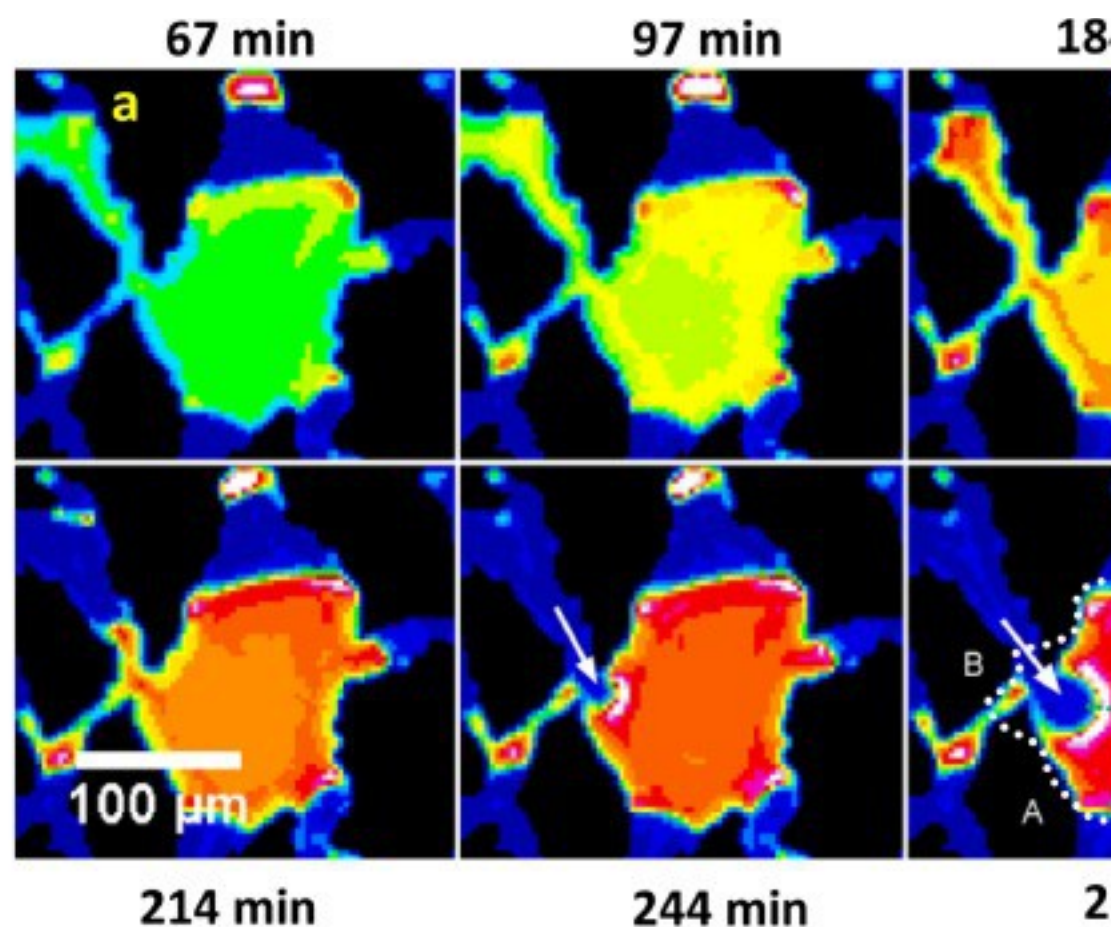
Fig. 8. Time-lapse images of pH for (a) Pore 2 and (c) Cluster 2 with large a_{it} values caused by invasion of scCO$_2$ bubbles. Also shown are (b) the transient profile of pixel pH along transect A-A' for Pore 2 and (d) temporal change in average pH for Pore 2 and Cluster 2. The short pink lines in (a) indicate scCO$_2$-water interfaces and the white

dotted line in (c) bounds the water-filled cluster. The arrows in (a) and (c) indicate the direction of the moving scCO$_2$-water interface during scCO$_2$ invasion.

Similarly, a large scCO$_2$ bubble invaded Cluster 2, leading to three segregated water bodies located in regions next to pore throats (Fig. 8c). In less than two hours, the pH decreased to its minimum value because of the enlarged area-to-volume ratio from 0.0072/μm to 0.056/μm. For both Pore 2 and Cluster 2, scCO$_2$dissolution and dsCO$_2$ mass transfer were significantly enhanced after invasion of scCO$_2$ bubbles into water-filled pores and increase of the associated a_{it} values (Fig. 8d), showing the importance of interplay between scCO$_2$ displacement and dissolution. Here, due to quite unpredictable pore-scale two-phase flow, we did not capture the fast changes in the area-to-volume ratio and the pH rate of changes that might occur within a smaller time window than the 30 min between 184 and 214 min. However, by observing the two data points for the change rate for Pore 2 after scCO$_2$ bubble invasion, we think the actual average peak rate for Cluster 2 may not be far away from our calculated value.

3.4. Diffusion-limited mass transfer

A single pore (P3 in Fig. 4) with a medium a_{it} (0.022/μm), relative to those of the four water-filled pores or pore clusters above, was used to investigate diffusion-limited mass transfer (Fig. 9). The single large pore was occupied by both water and scCO$_2$ with a stable interface. The water body within Pore 3 was also in contact with stable scCO$_2$-water interfaces at three large pore throats, while scCO$_2$ invaded slowly into the pore through a moving interface at a larger pore throat (marked by the arrow in Fig. 9a). During the first 214 min of injection, the relatively uniform pH decreased with time in the water body and along cross sections A-A' and B-B', with a small pH gradient from the scCO$_2$-water interfaces along A-A'. After a small scCO$_2$ bubble invasion occurred at 244 min, a pH gradient along B-B' between the newly established interface (with a pH lower than 4.00) and the pore center (with an average pH of 5.60) is observed (Fig. 9b), indicating the diffusion-limited mass transfer in this configuration with a medium a_{it}. In this case, the average pH decreased from 6.21 to 5.74 during the first 214 min, at a rate increasing from −0.0047/min at 97 min to −0.0033/min at 214 min, and continued to decrease at an increased rate as the pH approached 4.00 (see Fig. 9c).

67 min **97 min** **18**

214 min **244 min** **2**

100 μm

A-A'

b

67 min
97 min
184 min
214 min
244 min
274 min

B-B'

c

Fig. 9. (a) Time-lapse images showing water pH changes, (b) temporal pH profiles along transects A-A' and B-B', and (c) temporal decrease of average pH for a large water-filled pore (Pore 3) with a medium a_{it} value. The arrows in (a) indicate the direction of the moving scCO$_2$-water interface with scCO$_2$ invasion. The white dotted line shows the boundary of the water-filled pore.

3.5. Analysis of a_{it} effects on dissolution and mass transfer

The computed (absolute) pH rate of change as a function of time for the five selected pores or clusters are shown in Fig. 10a, and the correlation between these rates and the a_{it} values are presented in Fig. 10b. The rates are computed by dividing the observed, absolute pH difference by the time difference for two consecutive imaging times. For Pore 1 and Cluster 1, the calculated average rates for the entire experiment are 4.75×10^{-4}/min and 1.15×10^{-3}/min for a_{it} values of 0.0039/μm and 0.0061/μm, respectively. For Pore 2 and Cluster 2, the average rate and a_{it} are 1.14×10^{-3}/min and 0.0048/μm, and 2.70×10^{-3}/min and 0.0072/μm, respectively, before invasion of scCO$_2$ bubbles into the water-filled pore and cluster. These rates are similar to the values computed for Pore 1 and Cluster 1. After the bubble invasion, both the rate and a_{it} increased significantly (Fig. 10a). For Pore 2, the peak rate increased to 2.88×10^{-2}/min when the pH decreased from 5.46 to 4.60 within 30 min, with an a_{it} of 0.028/μm at 184 min. For Cluster 2, the peak rate increased to 5.84×10^{-2}/min for pH decreases from 5.59 to 3.98 within 30 min between the two images at 184 min and 214 min, with an a_{it} of 0.056/μm estimated at 184 min. For Pore 3, the rate decreased with time from 4.73×10^{-3}/min to 1.76×10^{-3}/min, illustrating the decline in concentration gradients over time, as the a_{it} value only changed from 0.016 to 0.022/μm. A linear trend between pH rate of change and a_{it} is observed for the seven data points (two data points each for Pore 2 and Cluster 2) from the five selected pores and clusters, indicating that a_{it}, representing the configuration of scCO$_2$-water phase interfaces in water-filled pores and pore clusters, plays an important role in pore-scale scCO$_2$ dissolution and dsCO$_2$ mass transfer. When the a_{it} value is small, rate-limited mass transfer prevails. When a_{it} is large, fast mass transfer dominates at the pore scale, potentially allowing for equilibrium to occur quickly. For a medium a_{it}, diffusion-limited mass transfer is observed, with a transient effect of concentration gradients on the pH rate of change, as the pH approaches its minimum value. The seemingly linear trend may indicate that a pore configuration with a small a_{it} may limit the mass transfer, leading to a slow increase in

dsCO$_2$ concentration, while that with a much larger a_{it} may result in an increase in dsCO$_2$ concentration orders of magnitude higher.
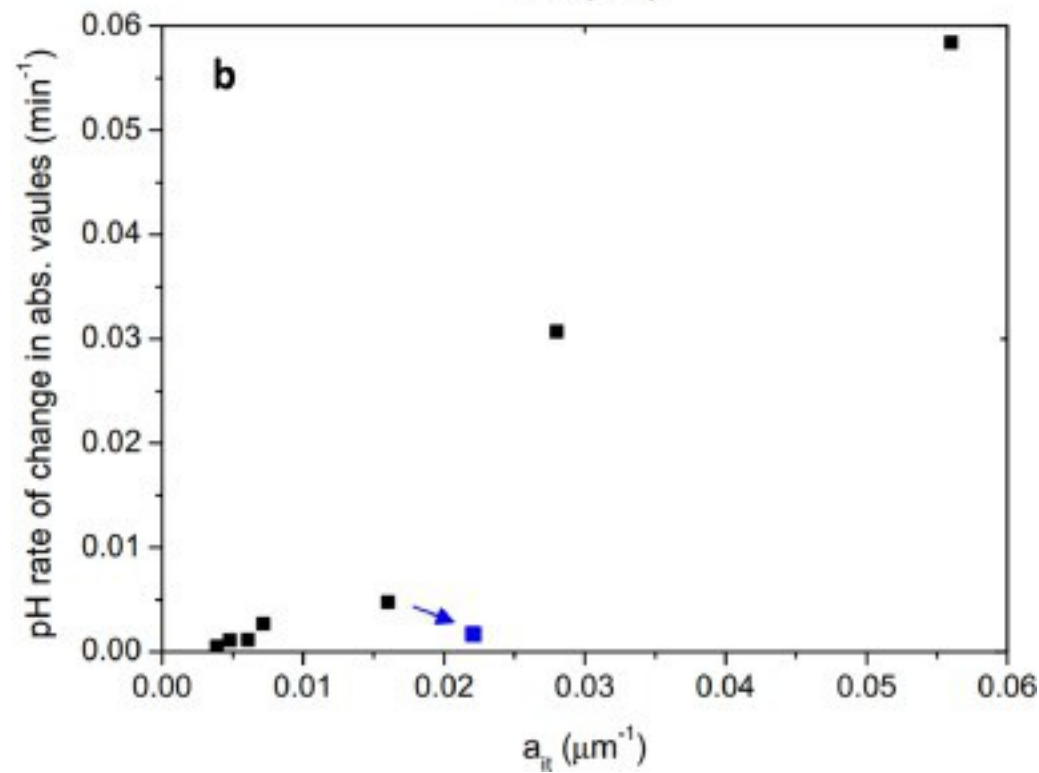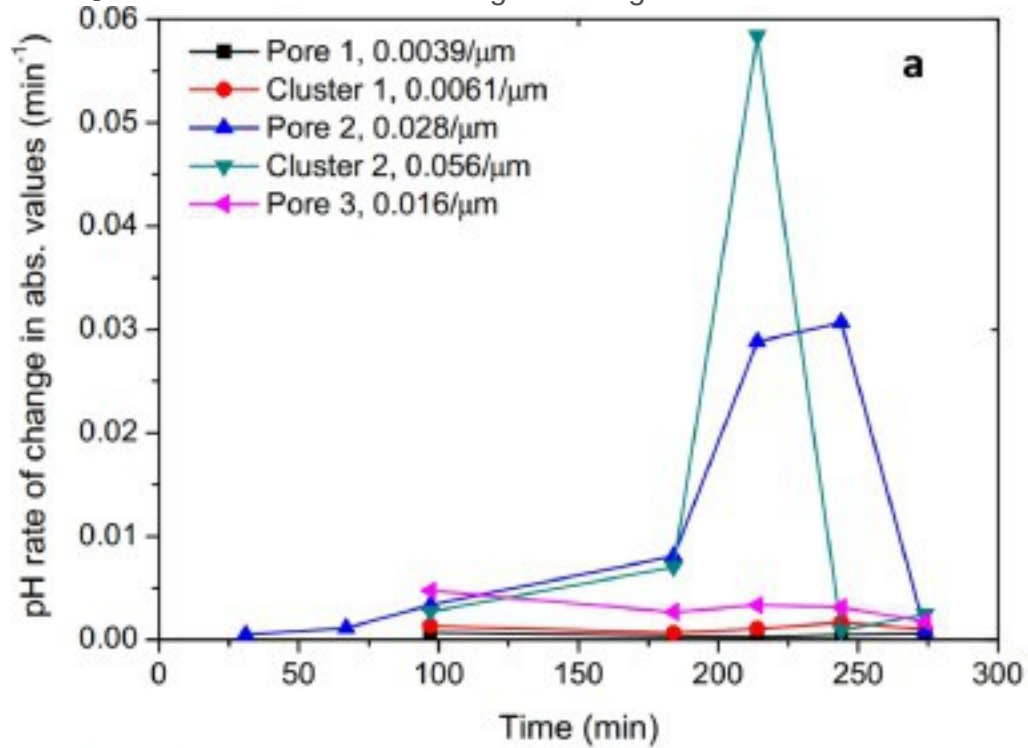
1. Download high-res image (272KB)
2. Download full-size image

Fig. 10. Effect of a_{it} on the time-dependent absolute rates of changes in pH: (a) average pH rate of change vs. time for the five selected pores and clusters, (b) correlation between the average rates of change and a_{it}, with the transient effect of concentration gradient on the pH rate of change for the diffusion-limited mass transfer (the blue arrow and square) in Pore 3. (For interpretation of the references to color in this figure legend, the reader is referred to the web version of this article.)

In addition to the five representative water-filled pores and pore clusters discussed so far, the statistics for over 100 selected water-filled pores and clusters were analyzed by calculating their average pH and a_{it} values at different times. The selected pores and clusters volumes were all higher than 87,500 μm^3 and had widths larger than the micromodel depth of 35 μm. Fig. 11 shows the relationship between pH and a_{it} at four different times (10, 67, 184, 274 min), as well as the relative computed concentration of dsCO$_2$ to its solubility (Spycher et al., 2003). For each time, the pH decreases and dsCO$_2$ concentration increases with the increase in a_{it}.
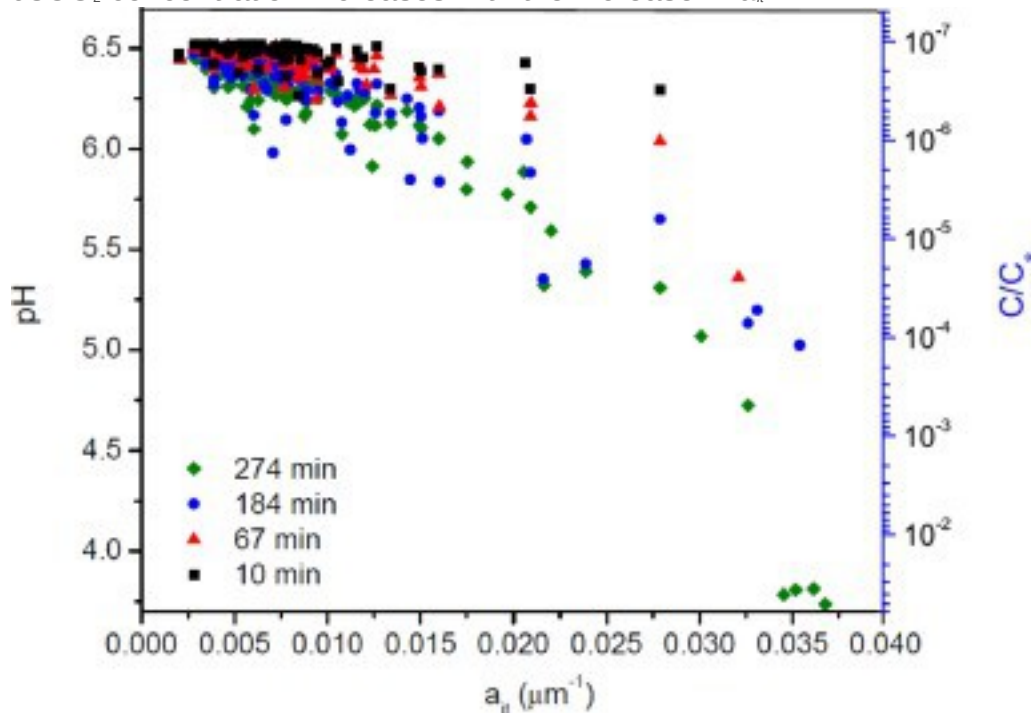
1. Download high-res image (146KB)
2. Download full-size image

Fig. 11. Relationship of average water pH and dsCO$_2$ concentration as a function of a_{it} for over 100 water-filled pores and clusters at different times. C$_s$ refers to the CO$_2$ solubility under experimental conditions.

It is clear from Figs. 10 and 11 that the pH is not linear with the area-to-volume ratio for a given dissolution time. This indicates that the pH decreases with a_{it} at a slower rate at

a small a_{it} than at a larger a_{it}. For very large value of a_{it}, the pH decreases rapidly, leading to quick equilibrium. For a very small value of a_{it}, both the pH and $dsCO_2$ concentration change at a very slow rate. A similar complicated relationship between normalized PCE effluent concentration and specific interfacial area (i.e., a_{it} in our study) was observed by Cho et al. (2005)using columns packed with different grain sizes of sand, although their a_{it} value ranged from 28 to 110 cm^{-1}, which is reasonable for unconsolidated sands. Their values are orders of magnitude higher than our values for the consolidated sandstone analogue used in our experiments. They observed that effluent concentration initially increased in a logarithmic trend for the homogeneous media/NAPL distribution conditions used in their study. On the other hand, quick disappearance in seconds of gaseous CO_2 bubbles in pore bodies was observed by Buchgraber et al. (2012) using micromodels with large pore throats. Because of the nonlinear relationship between a_{it} and the temporal change of $dsCO_2$concentration, standard modeling based on diffusive flux at the $scCO_2$-water interfaces may not able to reproduce the observed behavior of $scCO_2$ dissolution and $dsCO_2$ mass transfer.

4. Conclusions and implications

Experiments of $scCO_2$ dissolution and $dsCO_2$ mass transfer were conducted by injecting $scCO_2$ into a dyed water-saturated micromodel free of $dsCO_2$ at 9.0 MPa and 40°C. The 7.1 mm × 5.3 mm pore network, fabricated on the basis of a real sandstone core from a storage site, consisted of spatially heterogeneous (but chemically homogeneous) pores, pore throats, and clusters of pores and throats. The experiments lasted 4.5 h, resulting in reproducible residual water saturation distribution with average values ranging from 0.18~0.20, primarily consisting of water-filled pores and clusters by-passed by injected $scCO_2$. The concentration of $dsCO_2$ in these water-filled pores and clusters was imaged and tracked using pHrodo Red, a fluorescent pH indicator with a one-to-one relationship between water intensity and pH, from neutral down to a value of 3.70. Although the lowest reliable pH value for this dye is 0.6 units larger than the pH at full solubility, the application is still useful because the dye covers a pH large range (neutral to 3.7) during $scCO_2$ injection. So far, no other pH-dependent dye has been described in the literature for pore-scale experimental studies involving water and $scCO_2$, justifying presentation of our experimental results.

Through time-lapse high-resolution (1.62 μm × 1.62 μm/pixel) images, we observed that (1) pH values at each time are non-uniform, varying from 6.5 to 3.7, and (2) average pH values gradually decrease over time, with less than 1% reaching the minimum value by the end of the experiment. An analysis of five individual pores and clusters indicates that

pore-scale $scCO_2$ dissolution at phase interfaces and diffusion of dissolved $dsCO_2$ from these interfaces to pore centers are two relative fast processes, but that the mass transfer of $dsCO_2$ from the interfaces into the pores is controlled by restricted transport in long and narrow pore throats.

The rate of absolute change of pH with time depends mainly on the ratio between the area of phase interfaces available for dissolution and the volume of water-filled pores and clusters. Specifically, rate-limited mass transfer and slow pH changes prevail in the case of small a_{it} values, when a water-filled pore or cluster is surrounded by $scCO_2$-water interfaces at narrow pore throats. However, faster $scCO_2$ dissolution and phase equilibrium occurs when $scCO_2$ bubbles invade into a water-filled pore or cluster, significantly enhancing a_{it}. Diffusion-limited mass transfer occurs in the case of medium a_{it}. For the entire model domain, the unfavorable small a_{it} dominant in water-filled pores and clusters results in overall slow $scCO_2$ dissolution and mass transfer. This phenomenon is expected to be more pronounced in a large 3D system with highly heterogeneous pore-throat configurations and large clusters of pores by-passed by injected $scCO_2$. This direct observation of $scCO_2$ dissolution and $dsCO_2$ mass transfer at the pore scale is consistent with previous core-scale observations, demonstrating that the assumption of equilibrium $scCO_2$ dissolution may not be valid when the time scale to reach solubility is significantly larger than that of the problem of interest. The time scale to reach solubility is expected to increase with spatial scale of interest.

The observed dynamic, non-equilibrium dissolution and the inferred effect of area-to-volume ratios representing pore configurations may have implications to relevant dissolution processes at the field. Field-scale $scCO_2$ plumes often exhibit channelized $scCO_2$ distributions in high-permeability zones and by-passing of low-permeability zones at multiple scales, as observed at the Shenhua storage site (Chang et al., 2013, Zhang et al., 2016), the Frio pilot test site (Xu et al., 2010), and the Cranfield large-scale demonstration site (Hosseini et al., 2013) among others. Because of slow diffusion into the $scCO_2$-free low-permeability zones, $scCO_2$ dissolution and mass transfer in heterogeneous aquifers may have a significantly smaller role in solubility trapping than in homogeneous formations. The non-equilibrium $scCO_2$ dissolution at the boundaries between $scCO_2$ plumes and underlying brine regions may slow down the onset of convective mass transfer and reduce the stable mass-transfer rate, which has been numerically investigated (Gholami et al., 2015). The observed spatial variability in water pH may have some effects on chemical interactions in CO_2-water-mineral systems. All these impacts of dynamic dissolution may have complicated implications to field-scale geological carbon storage.

Acknowledgments

Appendix. Supplementary materials

Research data for this article

Open Data

for download under the CC BY licence

application 1

(DOCX, 110KB)

Download data

About research data

References

Agartan et al., 2015

E. Agartan, L. Trevisan, A. Cihan, J.T. Birkholzer, Q. Zhou, T.H. Illangasekare**Experimental study on effects of geologic heterogeneity in enhancing dissolution trapping of supercritical CO2**

Water Resour. Res., 51 (2015), pp. 1635-1648

http://dx.doi.org/10.1002/2014WR015778

CrossRefView Record in Scopus

Aggelopoulos and Tsakiroglou, 2012

C.A. Aggelopoulos, C.D. Tsakiroglou**Effects of micro-heterogeneity and hydrodynamic dispersion on the dissolution rate of carbon dioxide in water-saturated porous media**

Int. J. Greenhouse Gas Control, 10 (2012), pp. 341-350

ArticleDownload PDFView Record in Scopus

Akbarabadi and Piri, 2013

M. Akbarabadi, M. Piri**Relative permeability hysteresis and capillary trapping characteristics of supercritical CO_2/brine systems. An experimental study at reservoir conditions**

Adv. Water Resour., 52 (2013), pp. 190-206

ArticleDownload PDFView Record in Scopus

Backhaus et al., 2011

S. Backhaus, K. Turitsyn, R.E. Ecke**Convective instability and mass transport of diffusion layers in Hele-Shaw geometry**

Geophys. Res. Lett., 106 (2011), Article 104501, 10.1103/PhysRevLett.106.104501

CrossRef

Berg et al., 2013

S. Berg, S. Oedai, H. Ott**Displacement and mass transfer between saturated and unsaturated CO_2-brine systems in sandstone**

Int. J. Greenhouse Gas Control, 12 (2013), pp. 478-492

ArticleDownload PDFView Record in Scopus

Birkholzer et al., 2015

J.T. Birkholzer, C.M. Oldenburg, Q. Zhou**CO_2 migration and pressure evolution in deep saline aquifers**

Int. J. Greenhouse Gas Control, 40 (2015), pp. 203-220

ArticleDownload PDFView Record in Scopus

Buchgraber et al., 2012

M. Buchgraber, A.R. Kovscek, L.M. Castanier**A study of microscale gas trapping using etched silicon micromodels**

Transp. Porous Med., 95 (2012), pp. 647-668

CrossRefView Record in Scopus

Chang et al., 2013

C. Chang, Q. Zhou, L. Xia, X. Li, Q. Yu**Dynamic displacement and non-equilibrium dissolution of supercritical CO_2 in low permeability sandstone: an experimental study**

Int. J. Greenhouse Gas Control, 14 (2013), pp. 1-14

ArticleDownload PDFCrossRefView Record in Scopus

Chang et al., 2014

C. Chang, Q. Zhou, J. Guo, Q. Yu**Supercritical CO_2 dissolution and mass transfer in low-permeability sandstone: effect of concentration difference in water-flood experiments**

Int. J. Greenhouse Gas Control, 28 (2014), pp. 328-342

ArticleDownload PDFView Record in Scopus

Chang et al., 2016

C. Chang, Q. Zhou, T.J. Kneafsey, M. Oostrom, T.M. Wietsma, Q. Yu**Pore-scale supercritical CO_2 dissolution and mass transfer under imbibition conditions**

Advances in Water Resources, 92 (2016), pp. 142-158

ArticleDownload PDFView Record in Scopus

Cho et al., 2005

J. Cho, M.D. Annable, P.S.C. Rao**Measured mass transfer coefficients in porous media using specific interfacial area**

Environ. Sci. Technol., 39 (2005), pp. 7883-7888

CrossRefView Record in Scopus

Chomsurin and Werth, 2003

C. Chomsurin, C.J. Werth**Analysis of pore-scale nonaqueous phase liquid dissolution in etched silicon pore networks**

Water Resour. Res., 39 (9) (2003), pp. 1265-1275, 10.1029/2002WR001643

View Record in Scopus

Ennis-King and Paterson, 2003

J. Ennis-King, L. Paterson**Role of convective mixing in the long-term storage of carbon dioxide in deep saline formations**

Paper SPE 84344, Presented at the SPE Annual Technical Conference and Exhibition, Denver, CO, USA (2003)

Ennis-King-and-Pate

r
s
o
n
,
-
2
0
0
5

J. Ennis-King, L. Paterson**Role of convective mixing in the long-term storage of carbon dioxide in deep saline formations**
SPE J., 10 (3) (2005), pp. 349-356
CrossRefView Record in Scopus

Gholami
et al.,
2015

Y. Gholami, R. Azin, R. Fatehi, S. Osfouri, A Bahadori**Prediction of carbon dioxide dissolution in bulk water under isothermal pressure decay at different boundary conditions**
J. Mol. Liq., 202 (202) (2015), pp. 23-33
ArticleDownload PDFView Record in Scopus

Hosseini et al.,
2013

S.A. Hosseini, H. Lashgari, J.W. Choi, J.P. Nicot, J. Lu, S.D. Hovorka**Static and dynamic reservoir modeling for geological CO_2 sequestration at Cranfield, Mississippi, USA**
Int. J. Greenhouse Gas Control, 18 (5) (2013), pp. 449-462
ArticleDownload PDFView Record in Scopus

IPCC 2005

IPCC**Special Report on Carbon Dioxide Capture and Storage**
B. Metz, O. Davidson, H.C. de Coninck, M. Loos, L.A. Meyer (Eds.), Prepared by Working Group III of the Intergovernmental Panel on Climate Change, Cambridge, New York, NY(2005), p. 442
View Record in Scopus

Kneafsey and Pr

T.J. Kneafsey, K. Pruess**Laboratory flow experiments for visualizing carbon dioxide-induced, density-driven brine convection**
Transp. Porous Media, 82 (1) (2010), pp. 123-139
CrossRefView Record in Scopus

Krevor et al., 201

S.C.M. Krevor, R. Pini, L. Zuo, S.M. Benson**Relative permeability and trapping of CO_2 and water in sandstone rocks at reservoir conditions**

Water Resour. Res., 48 (2012)

Life Technologies

Life Technologies Website. http://www.lifetechnologies.com/us/en/home.html.

MacMinn et al., 2

C.W. MacMinn, J.A. Neufeld, M.A. Hesse, H.E. Huppert**Spreading and convective dissolution of carbon dioxide in vertically confined, horizontal aquifers**

Water Resour. Res., 48 (2012), p. W11516, 10.1029/2012WR012286

Neufeld et al., 20

J.A. Neufeld, M.A. Hesse, A. Riaz, M.A. Hallworth, H.A. Tchelepi, H.E. Huppert**Convective dissolution of carbon dioxide in saline aquifers**

Geophys. Res. Lett., 37 (2010), p. L22404, 10.1029/2010GL044728

Pau et al., 2010

G.S. Pau, J.B. Bell, K. Pruess, A.S. Almgren, M.J. Lijewski, K. Zhang**High resolution simulation and characterization of density-driven flow in CO_2 storage in saline aquifers**

Adv. Water Resour., 33 (4) (2010), pp. 443-455

ArticleDownload PDFView Record in Scopus

Pini and Benson

R. Pini, S.M. Benson**Simultaneous determination of capillary pressure and relative permeability curves from core-flooding experiments with various fluid pairs**

Water Resour. Res., 49 (6) (2013), pp. 3516-3530

CrossRefView Record in Scopus

Pini and Benson

R. Pini, S.M. Benson**Characterization and scaling of meso-scale heterogeneities in sandstones**

Geophys. Res. Lett., 40 (15) (2013), pp. 3903-3908

CrossRefView Record in Scopus

Pini et al., 2012

R. Pini, S.C.M. Krevor, S.M. Benson**Capillary pressure and heterogeneity for the CO_2/water system in sandstone rocks at reservoir conditions**

Advances in Water Resources, 38 (2012), pp. 48-59

ArticleDownload PDFView Record in Scopus

Pruess and Spyc

K Pruess, N Spycher**ECO2N – A fluid property module for the TOUGH2 code for studies of CO_2 storage in saline aquifers**

Energ Convers Manage, 48 (6) (2007), pp. 1761-1767

ArticleDownload PDFView Record in Scopus

Rasband, 1997-2

W.S Rasband**ImageJ**

U. S. National Institutes of Health, Bethesda, Maryland, USA (1997, 2014)

http://imagej.nih.gov/ij/

Riaz et al., 2006

A. Riaz, M. Hesse, H.A. Tchelepi, F.M. Orr**Onset of convection in a gravitationally unstable diffusive boundary layer in porous media**

J. Fluid Mech., 548 (1) (2006), pp. 87-111

CrossRefView Record in Scopus

Rodriquez de Ca

A Rodriquez de Castro, N. Shokri, N. Karadimitriou, M. Oostrom, V. Joekar-Niasar**Experimental study of non-monotonicity of capillary desaturation curves in a pore network**

Water Resour. Res., 51 (2015), [10.1002/2015WR017727](10.1002/2015WR017727)

Rodriguez de Ca

A Rodriguez de Castro, M. Oostrom, N. Shokri**Effects of shear-thinning fluids on residual oil formation in microfluidic pore networks**

J. Colloid and Interface Science, 472 (2016), pp. 34-43, 10.1016/j.jcis.2016.03.027

ArticleDownload PDFView Record in Scopus

Senel et al., 201

O. Senel, R. Will, R.J. Butsch**Integrated reservoir modeling at the Illinois Basin – Decatur project**

Greenhouse Gases: Sci. Technol., 4 (5) (2014), pp. 662-684

CrossRefView Record in Scopus

Shi et al., 2011

J.Q. Shi, Z. Xue, S. Durucan**Supercritical CO_2 core flooding and imbibition in Tako sandstone-influence of sub-core scale heterogeneity**

Int. J. Greenhouse Gas Control, 5 (2011), pp. 75-87

ArticleDownload PDFView Record in Scopus

Spycher et al., 2

N. Spycher, K. Pruess, J. Ennis-King**CO_2–H_2O mixtures in the geological sequestration of CO_2. I. Assessment and calculation of mutual solubilities from 12 to 100 °C and up to 600 bar**

Geochim Cosmochim Acta., 67 (16) (2003), pp. 3015-3031

ArticleDownload PDFView Record in Scopus

Spycher and Pru

N Spycher, K Pruess**CO_2–H_2O mixtures in the geological sequestration of CO_2. II. Partitioning in chloride brines at 12–100 °C and up to 600 bar**

Geochim Cosmochim AC, 69 (13) (2005), pp. 3309-3320

ArticleDownload PDFView Record in Scopus

Wang et al., 201

Y. Wang, C. Zhang, N. Wei, M. Oostrom, T.W. Wietsma, X. Li, A. Bonneville**Experimental study of crossover from capillary to viscous fingering for supercritical CO_2–water displacement in a homogeneous pore network**
Environ. Sci. Technol., 47 (2013), pp. 212-218
CrossRefView Record in Scopus

Willingham et al.

T.W. Willingham, C.J. Werth, A.J. Valocchi**Evaluation of the effects of porous media structure on mixing-controlled reactions using pore-scale modeling and micromodel experiments**
Environ. Sci. Technol., 42 (9) (2008), pp. 3185-3193
CrossRefView Record in Scopus

Xu et al., 2010

T. Xu, Y.K. Kharaka, C. Doughty, B.M. Freifeld, T.M. Daley**Reactive transport modeling to study changes in water chemistry induced by CO_2injection at the Frio-I brine pilot**
Chem. Geol., 271 (3) (2010), pp. 153-164
ArticleDownload PDFView Record in Scopus

Zhang et al., 201

C. Zhang, M. Oostrom, J.W. Grate, T.W. Wietsma, M.G. Warner**Liquid CO_2 displacement of water in a dual-permeability pore network micromodel**
Environ. Sci. Technol., 45 (2011), pp. 7581-7588
CrossRefView Record in Scopus

Zhang et al., 201

K. Zhang, J. Xie, C. Li, L. Hu, X. Wu, Y. Wang**A full chain CCS demonstration project in northeast Ordos Basin, China: operational experience and challenges**
Int. J. Greenhouse Gas Control, 50 (2016), pp. 218-230
ArticleDownload PDFView Record in Scopus

Zhou et al., 2008

Q. Zhou, J.T. Birkholzer, C.F. Tsang, J. Rutqvist**A method for quick assessment of CO_2 storage capacity in closed and semi-closed saline aquifers**
Int. J. Greenhouse Gas Control, 2 (2008), pp. 626-639
ArticleDownload PDFView Record in Scopus

Zhou et al., 2010

Q. Zhou, J.T. Birkholzer, E. Mehnert, Y.F. Lin, K. Zhang**Modeling basin- and plume-scale processes of CO_2 storage for full-scale deployment**
Ground Water, 48 (4) (2010), pp. 494-514
View Record in Scopus

Zuo et al., 2013

L. Zuo, C. Zhang, R.W. Falta, S.M. Benson**Micromodel investigations of CO_2 exsolution from carbonated water in sedimentary rocks**
Adv. Water Resour., 53 (2013), pp. 188-197